Nondestructive Testing and Evaluation

ISSN: (Print) (Online) Journal homepage: www.tandfonline.com/journals/gnte20

Splitting frequency behavior of wireless power transfer for eddy current testing applications

Lawal Umar Daura, Monika Roopak, Gui Yun Tian, Simon Parkinson, Xiaotian Chen & Emmanuel Tashiwa Ibrahim

To cite this article: Lawal Umar Daura, Monika Roopak, Gui Yun Tian, Simon Parkinson, Xiaotian Chen & Emmanuel Tashiwa Ibrahim (31 Mar 2025): Splitting frequency behavior of wireless power transfer for eddy current testing applications, Nondestructive Testing and Evaluation, DOI: 10.1080/10589759.2025.2477682

To link to this article: https://doi.org/10.1080/10589759.2025.2477682

© 2025 The Author(s). Published by Informa UK Limited, trading as Taylor & Francis Group.

Published online: 31 Mar 2025.

Submit your article to this journal

Article views: 64

View related articles

View Crossmark data

Full Terms & Conditions of access and use can be found at
https://www.tandfonline.com/action/journalInformation?journalCode=gnte20

NONDESTRUCTIVE TESTING AND EVALUATION
https://doi.org/10.1080/10589759.2025.2477682

Taylor & Francis
Taylor & Francis Group

OPEN ACCESS Check for updates

Splitting frequency behavior of wireless power transfer for eddy current testing applications

Lawal Umar Daura[a], Monika Roopak[b], Gui Yun Tian[c], Simon Parkinson[d], Xiaotian Chen[e] and Emmanuel Tashiwa Ibrahim[c]

[a]School of Physics, Engineering and Computer Science, University of Hertfordshire, Hatfield, UK; [b]Computer Science and Technology, University of Bedfordshire, Luton, UK; [c]School of Engineering, Newcastle University, Newcastle Upon Tyne, UK; [d]School of Computing & Engineering, University of Huddersfield, Huddersfield, UK; [e]School of Mechanical Engineering, Sichuan University, Zigong City, China

ABSTRACT

This paper presents a novel approach for Non-destructive Testing and Evaluation (NDT&E) of cracks in metallic structures using Eddy Current Testing (ECT) integrated with the resonance Wireless Power Transfer (WPT) concept. The proposed method enhances ECT for efficient power transfer between transmitter-receiver (Tx-Rx) coils and employs Gaussian Random Projection (GRP) for feature reduction, enabling real-time data processing. Experimental results on two aluminium material samples demonstrate the effectiveness of the proposed approach in localising and characterising slots, with an R^2-value/RMSE of 99.86%/0.06 mm for width and 99.38%/0.25 mm for depth slot parameters. The findings highlight the potential of this method for improving NDT&E of metallic structures.

ARTICLE HISTORY
Received 21 February 2024
Accepted 5 March 2025

KEYWORDS
Coils; Eddy current testing; feature extraction; magnetic resonance; gaussian random projection; wireless power transfer

1. Introduction

Metals have remained a fundamental component in various crucial industrial structures despite the development of multiple metal-like structures due to their unique properties that make them irreplaceable in different applications, making them an essential workhorse in our society's development [1]. However, exposure of metallic structure to external and internal causative factors while in service or due to ageing causes the formation of defects (cracks and corrosion), which weakens its microstructures. Such defects account for more than 90% of frequently occurring failures in engineering structures and aeroplanes [2], leading to loss of life and properties with huge financial losses. Non-Destructive Testing (NDT) quantitatively assesses such defects in metallic structures; effectively, safely, cheaply and reliably whilst the structure is in operation without negatively disturbing its serviceable functions, which simplifies preventive maintenance, among others.

Among the NDT sensors, this study employed an Eddy Current Testing (ECT) sensor [3] based on two separate transmission (Tx) and reception (Rx) coils, which operate by

CONTACT Lawal Umar Daura l.u.daura@herts.ac.uk

© 2025 The Author(s). Published by Informa UK Limited, trading as Taylor & Francis Group.
This is an Open Access article distributed under the terms of the Creative Commons Attribution License (http://creativecommons.org/licenses/by/4.0/), which permits unrestricted use, distribution, and reproduction in any medium, provided the original work is properly cited. The terms on which this article has been published allow the posting of the Accepted Manuscript in a repository by the author(s) or with their consent.

measuring changes in electromagnetic fields passing through metallic objects. This sensor is chosen for its high sensitivity and non-invasive nature, making it ideal for non-destructive testing applications. However, the ECT has been developing, for decades, from single frequency to multiple frequencies, pulsed, and sweep frequency excitation. The response of sweeping frequencies ECT excitation can provide optimal resonance frequencies for maximum energy transfer at an improved signal-to-noise ratio, as well as multiple-layer information. The Tx-Rx coils probe used in sweep frequency ECT has weak induction at very low frequencies, resulting in low eddy current density transfer to the Rx coil; a weaker detection signal. This leads to lower detection sensitivity and fewer feature points, posing a challenge to conventional sweep frequency ECT. Therefore, this paper integrates magnetically coupled resonant Wireless Power Transfer (WPT) concepts of charging electric vehicles and the ECT technique to modify the Tx-Rx probe for multiple resonances response when operating in an over-coupled region of operation [4]. The WPT concept operates at maximum energy to overcome low energy transfer issues, provides splitting frequency from the multiple resonance response for multiple feature points [4], and has the availability of integrated circuit (IC) chips for signal processing [5]. The magnetically coupled resonant WPT-based ECT (WPTECT) technique uses a magnetically coupled resonant behaviour of Tx-Rx coils to efficiently transfer energy similar to the resonant non-radiative WPT of charging electric vehicles [6].

Compared to other ECT techniques, the novel Tx-Rx WPTECT provides multiple resonance frequency responses for various feature points [7]. It combines the advantages of different WPT topologies and other inductively coupled Tx-Rx ECT methods. Additionally, the use of sweep frequency excitation allows for the collection of information on different penetration depths and defect parameters, which cannot be achieved using the traditional single-frequency ECT method [8]. Similarly, it overcomes the issue of shorter testing time with less power in each frequency component, as exhibited by multiple-frequency ECT [3]. In comparison to pulsed ECT [9], which reduces measuring time and covers a broad spectrum of frequency components [10], it still has issues with coupling variation and response distortion caused by non-resonance harmonic frequency contents. The broad frequency spectrum of pulse excitation causes some attenuation of the inductively coupled Tx-Rx coils due to the presence of fundamental and other non-resonance frequency harmonic currents, altering the influence of opposing induced-eddy-current field from the sample. The recent EC testing explored sweep frequency excitation and natural resonance features for crack quantification [11], detection of thickness, measurement of permeability and conductivity of materials coating [12–14], and more complex information about metallic object detection [13,15]. The advantage of sweep frequency excitation ECT using a fixed probe position enables testing of complicated areas where scanning is impossible. However, it is blind to defect location [16] and operates at a decreasing (single resonance) frequency with increasing response magnitude for higher crack depth [11,12].

The previous magnetic resonance Tx-Rx WPTECT provided multiple feature extraction points, including response shape feature reduction techniques like principal component analysis (PCA) and Deep Learning feature fusion from the response of series-series, parallel-parallel or a combination of series and parallel circuit topologies of WPT [17–19]. However, the performance of multiple feature points for slot characterisation is not as effective as that of PCA and Deep Learning feature fusion [18]. Furthermore, the

PCA feature reduction is computationally expensive and slow compared to other unsupervised Machine Learning methods. Therefore, this paper proposes the Machine Learning–based Gaussian Random Projection (GRP) as a feature reduction technique due to its computational efficiency, data independence ideal for real-time data processing, and its ability to resonance point features.

In this paper, we propose design and development of an advanced circuit topology of WPTECT to study the impact of cracks on aluminium material. This advanced circuit combines the advantages of parallel and series basic compensation topologies in each primary and secondary unit of the WPTECT for efficient response and multiple feature points. We also use Machine Learning–based GRP feature extraction to dimensionally reduce the signal response of the advanced circuit topology, along with multiple resonance point feature extraction. In this paper, we compare the performance of the extracted GRP features with those of the resonance point features and PCA feature reduction techniques.

The paper is organised as follows: section 2 describes the concept of WPTECT consideration for slot characterisation and feature reduction by the GRP technique while section 3 describes the methods and experimental study employed. Section 4 is the analysis of the GRP technique feature extraction along with the resonance points and PCA features, while section 5 discusses the GRP features in comparison with other extracted features and the proposed study with other state-of-the-art literature for slot characterisation.

2. Review of WPTECT concept

The Massachusetts Institute of Technology (MIT) is credited with developing modern wireless power transfer (WPT) technologies, known as resonance inductive power transfer (RIPT), that revolutionised the way electric vehicles are charged in 2007 [6]. It is an improvement of the inductive coupling of the Tx-Rx WPT system which operates at maximum efficiency. The RIPT circuit eliminates the reactive power components by operating without leading or lagging between the current and voltage in each coil for optimal real power transfer [20,21]. The optimal real power is achieved by connecting multiple reactive elements, like capacitors and inductors, together in series and/or parallel, named the topology configuration of WPT [20]. The optimal real power maximises the magnetic field linking the Rx coil, which offers the advantage of not exposing the human body to ionising radiation because of its non-electric wave nature.

There are four basic compensating (reactance) topologies of magnetically coupled resonant WPT [22]. In each of the Tx and Rx coils of the WPTECT probe, a compensating reactance is connected to control their resonance frequency by modifying their quality factors to lower the Tx reactive power rating and cancel out the Rx inductance effect [20]. They include Series (S) or Parallel (P) resonant capacitor connection to Tx and Rx coils in the form of primary – secondary; SS, SP, PS or PP networks [20,23]. As discussed in [20,23,24], different topologies have different impedance matching and quality factor equations, leading to different WPTECT systems' measurement performances. The SS topology was applied for WPTECT to prove the concept by characterising the width and depths of slots [19] while the PP topology was applied for

dent area evaluation to compare different feature extraction including deep learning features [18]. Each topology has its qualities and limitations for application to NDT&E.

The SS topology provides low input and output impedance for a maximum current at resonance, leading to maximum field generation. In contrast, the PP topology compensation provides a higher efficiency transfer response to metal and defects with less sensitivity to noise influence due to its current source nature and higher input and out impedance at the resonance point [25]. However, with the potential of multiple resonances at lower Tx-Rx and sample coupling, the Tx coil spends a high reactive power for any of the basic WPT topologies due to reduced Tx-Rx and sample coupling. Thus, the Tx parallel capacitor suffers a higher voltage effect, while the series capacitor suffers a higher current effect while delivering the required reactive power [26]. Additionally, the Rx parallel capacitor requires a small Tx current to generate a high current in the resonant coil, leading to high-performance switches' requirements due to higher resonant voltage than Tx. In contrast, the Rx series capacitor requires a larger Tx current, which leads to low efficiency due to high Tx coil loss. Therefore, the load and source impedances to the Tx and Rx coils control the current utilisation in the Tx and Rx coils, respectively, including resonance behaviour and splitting frequency characteristics. Therefore, it is not practically wise to dependably implement series or parallel topology for the Tx coil, as each depends on the behaviour of specific application requirements [21].

Therefore, this study applies an advanced topology based on a combination of series and parallel capacitors compensation to each Tx and Rx network, as presented in Figure 1 PS-PS WPTECT hybrid circuit diagram. The circuit behaves as an S-S topology if Ca is zero and Cb is greater than zero. Otherwise, it behaves as a P-P topology if Ca is greater than zero and Cb is a very high value (infinity). The proposed PS-PS WPTECT harnesses the advantage of both S-S and P-P topologies for sensing applications. The benefit of PS-PS topology over basic topologies is reducing the effective reactance of the Tx coil by the series reactance (Xb) and reducing the stress on parallel reactance (Xa) as it only supplies a section of total reactive power to maintain the oscillation [26]. It also acts as a resonance compensation and impedance matching network at the same time.

The two coils, Tx and Rx inductors in Figure 1, coupled inductively with the inductance Ls of the metallic sample equivalent circuit, including its resistance

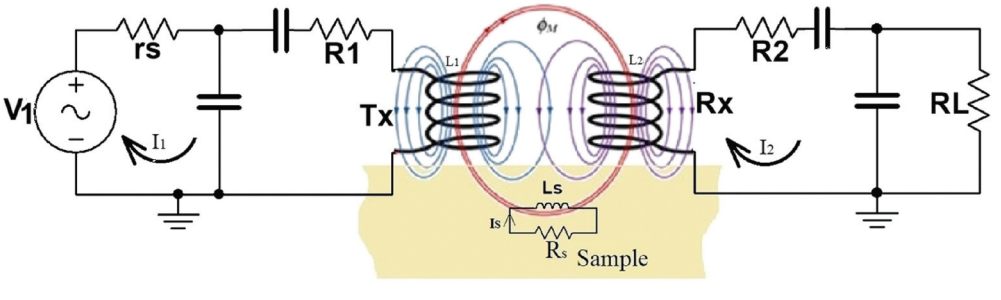

Figure 1. PS-PS (combination of S-S and P-p) topology of WPTECT circuit diagram.

(Rs) and the eddy current (Is). The impedances of the transmitter (Z1) and receiver (Z2) are, respectively, given by Equations (2.1) and (2.2). The three current loops in the circuit (Figure 1): Tx excitation current (I1), Rx induced-current (I2), and the sample induced-eddy-current (Is) are represented by Equations (2.4) by applying Kirchhoff's laws to the circuits. The inductance (Ls) of the metallic sample forms the eddy current (Is) loop with resistance Rs and couples inductively to the Tx and Rx inductors. Equation (2.4) is used to determine the dominant coil's parameters (self-inductance and -resistance) which vary according to the sample permeability, conductivity and geometric nature due to eddy-current interruption. The sample acts as an inductor through which the eddy current circulates. In Equation (2.4), M12, M1s, and M2s represent the mutual inductances for the Tx-Rx coils, Tx-sample and Rx-sample, respectively. These values depend on their appropriate coupling coefficients (K_{12}, K_{1S} and K_{2S},) and inductances (L1, L2 and Ls).

Additionally, Zs stands for the impedance of the metallic sample equivalent circuit. Equations (2.5) is derived from equation (2.4) by eliminating the last row to modify the Tx and Rx models' behaviour by including the influence of sample parameters, Rs, Ls, and mutual couplings, M1s and M2s. However, the Rs and Ls of the sample depend on defect parameters and sample geometry in addition to material type. Their influence affects the Tx and Rx impedances, hence the resonance frequency, which manifests in the voltage and current frequency responses. Moreover, at the point of defect, there is a change in permeability, conductivity and geometrical nature of the metallic sample which causes variation of the voltage and current, leading to a change in eddy current density before and after the defect. By evaluating Equations (2.5) in the absence of the metal sample, that is $M_{1s} = M_{2s} = 0$, the ratio of voltage across the load resistance, RL (V_{RL}) to that of the source voltage (V) is derived and given by equation (2.6). The ratio of the output to input excitation voltages is proportional to the scattering parameter, S21, given by Equations (2.7) [27] and has been evaluated for NDT&E in the previous WPTECT [18,19]. The scattering parameter (S21) has a better perception of measuring signal integrity at high frequency because of the skin depth problem. The S21 represents the forward voltage gain and is sometimes referred as the transmission coefficient [28]. The potential of multiple peaks of S_{21} response at a given range of frequency occurs at a higher Tx-Rx coupling above critical coupling in addition to the dependency on the WPT topology's input and output matching requirement.

$$Z_1 = r_s + \left(\frac{1}{j\omega Ca}\right)//\left(\left(\frac{1}{j\omega Cb}\right) + R_1 + j\omega L_1\right) \tag{2.1}$$

$$Z_2 = \left(R_2 + j\omega L_2 + \left(\frac{1}{j\omega Cb}\right)\right) + \left(\frac{1}{j\omega Ca}\right)//R_L \tag{2.2}$$

$$Z_s = R_s + j\omega L_s \tag{2.3}$$

$$\begin{pmatrix} V \\ 0 \\ 0 \end{pmatrix} = \begin{pmatrix} Z_1 & -j\omega M_{12} & -j\omega M_{1s} \\ -j\omega M_{12} & Z_2 & j\omega M_{2s} \\ -j\omega M_{1s} & j\omega M_{2s} & Z_s \end{pmatrix} \begin{pmatrix} I_1 \\ I_2 \\ I_s \end{pmatrix} \tag{2.4}$$

$$\begin{bmatrix} V(\omega) \\ 0 \end{bmatrix} = \begin{bmatrix} Z_1 + \frac{(\omega M_{1s})^2}{Z_s} & Z_{12} \\ Z_{21} & Z_2 + \frac{(\omega M_{2s})^2}{Z_s} \end{bmatrix} \begin{bmatrix} I_1 \\ I_2 \end{bmatrix} \tag{2.5}$$

Interchanging port1 to port2 and vice-versa of the proposed applied topology (Figure 1) shows that the PS-PS topology is a symmetrical ($Z_{11} = Z_{22}$.) and reciprocal network ($Z_{21} = Z_{12}$), The impedance parameters are derived in ref [18] using PP topology. Using the same matrix reduction from Equations (2.5).

$$\frac{V_{RL}(\omega)}{V(\omega)} = \frac{-j\omega M_{12} \cdot \left(\left(\frac{1}{j\omega Ca} \right) // R_L \right)}{\left(Z_1 Z_2 + (\omega M_{12})^2 \right)} \tag{2.6}$$

$$S_{21} = 2 \frac{V_{RL}(\omega)}{V(\omega)} \sqrt{\frac{r_s}{R_L}} \tag{2.7}$$

The application of WPT to ECT is based on the influence of the eddy current field on the power transfer between Tx and Rx according to Faraday's law of electromagnetic induction and Lenz's law. The primary magnetic field linking Rx passes through the metallic sample, modified by the EC-generated field, which carries information related to the permeability, conductivity, and geometrical nature of the metallic sample, and manifests in the features of the WPTECT response. To evaluate the extent to which these variables influence the PS-PS WPTECT topology response and feature extraction and selection, we simulated Figure 1 PS-PS WPTECT circuit topology using LTspice, and finally verified by experimental simulation for slot parameter estimation.

The response from LTSpice simulation of the PS-PS circuit topology of WPTECT is achieved by varying the sample inductance (Ls) and resistance (Rs) and mutual coupling between Tx-Rx coils and sample based on AC analysis for a frequency ranging from 1 MHz to 7 MHz. The Ls and Rs mimic the sample permeability and conductivity respectively and manifest in the S_{21} parameters for facilitating comparison with the experimental system.

Figure 2 depicts the S21 response for varying Ls, which is a function of the sample geometry and magnetic behaviour and Rs, which depends on the sample geometry and conductivity. The response of the dual peaks is affected by the change in mutual coupling, K12 from 0.9 to 0.94, as shown in Figure 2(a). The higher values of K12 are chosen because of the condition for splitting frequency achievement, which is at higher coupling between Tx and Rx coils [29]. It has also shown that the first peek (m1) of the dual response is more affected by the variation of Ls (4μH to 20μH) and Rs (10 mΩ to 90 mΩ), as seen in Figure 2(b,c), which is due to the extra power supply by the Tx coil to compensate for the eddy current losses [25]. The inset Figure 2(b) shows the variation of S21 for varying Ls and Figure 2(c) shows that of the variation of Rs. They are described by the decreasing and increasing behaviour of the S21 first peak due to the conductivity and permeability changes around the defects which

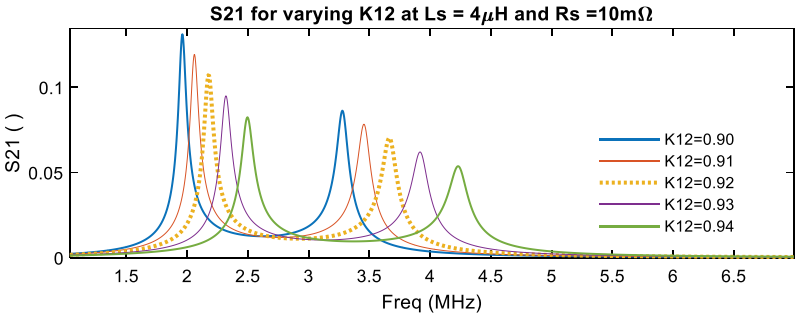

(a) Variation of mutual coupling

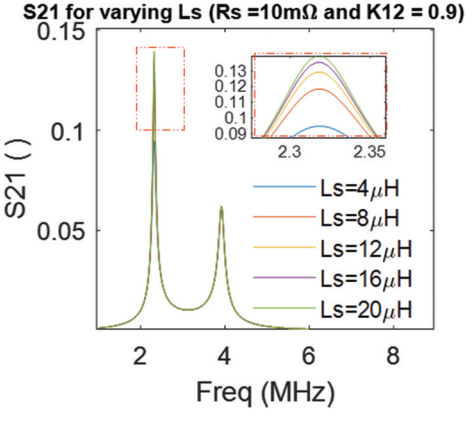

(b) Variation of sample inductance

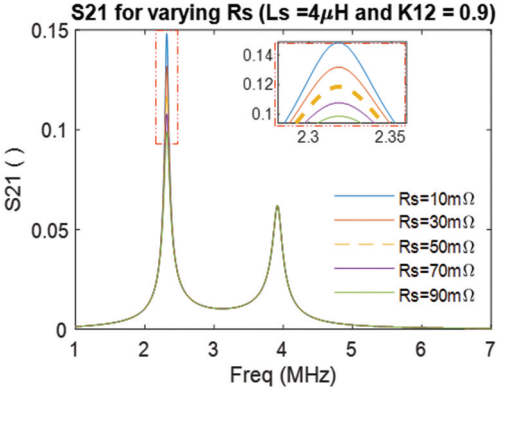

(c) Variation of sample resistance

Figure 2. S21 response of the WPTECT probe for varying sample parameters. (a) variation of mutual coupling with the sample, (b) variation of sample inductance (ls) and (c) variation of sample resistance (rs).

manifest in the extracted features. However, the lift-off effect contributes to the variation of K12, which shifts the magnitudes and frequencies of the dual peak response (Figure 2(a)).

To confirm the simulated results in Figure 2, the next sections provide the experimental procedures for our proposed PS-PS WPTECT system design, implementation and evaluation, including the comparison of the extracted feature performance for the characterisation of slot parameters on two aluminium materials.

3. Methodology

This section covers the details of the methods used for scanning two aluminium samples. It includes the design and configuration of the advanced PS-PS WPTECT probe, along with its simulation and experimental verification. The discussion also includes feature comparison for slot characterisation and comparison to state-of-the-art literature on slot characterisation with our proposed PS-PS WPTECT probe model.

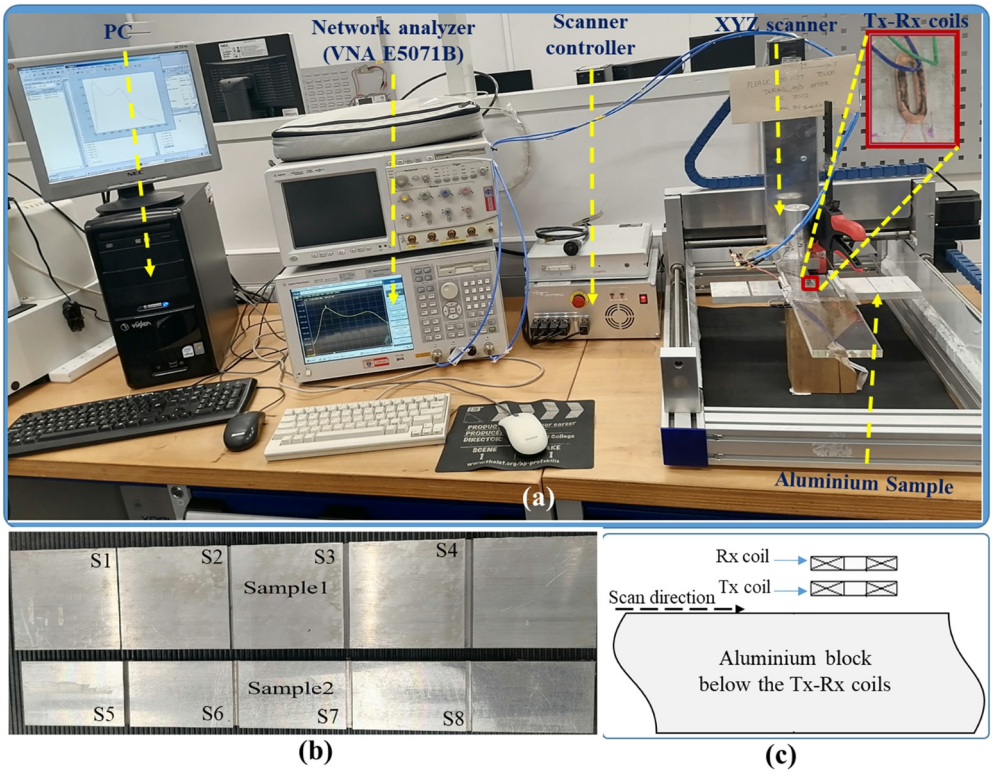

Figure 3. Experimental set-up (a) photograph of the instruments and peripheral components, (b) two aluminium block samples with eight slots, S1 – S8 (c) arrangement of tx-rx coils and scan direction on aluminium block sample.

Table 1. Slot parameters of different widths and depths data set.

Crack/Slot	S1	S2	S3	S4	S5	S6	S7	S8
Width (mm)	1.00	2.00	3.00	4.00	3.30	3.30	3.30	3.30
Depth (mm)	4.00	4.00	4.00	4.00	2.00	4.00	6.00	8.00

3.1. Sample preparation

In this experiment, two aluminium blocks are used. Each block contains four slots, making a total of eight slots labelled S1-S8, which were designed to resemble idealised cracks. The layout of these slots can be seen in Figure 3(b), while their specific parameters are listed in Table 1. The first block, called 'sampl1' measures 76.2 mm × 300 mm x 12.7 mm (width x length x thickness), and S1-S4 slots with widths of 1 mm, 2 mm, 3 mm, and 4 mm, respectively. These slots are evenly spaced 60 mm apart and have a depth of 4 mm each. The second block, called 'sample2', measures 50 mm × 300 mm x 10 mm and contains S5-S8 slots with depths of 2 mm, 4 mm, 6 mm and 8 mm, respectively. These slots are also evenly spaced 60 mm apart and have a width of 3.3 mm along the scan side.

3.2. Probe design and circuit configuration

The circuit design for the sensor probe involves a Tx-Rx coil configuration. The Tx coil generates an alternating magnetic field, which induces eddy currents in the metallic sample. The Rx coil detects changes in the magnetic field caused by the presence of cracks. The Tx and Rx coils are connected to the advanced WPT circuit, PS-PS topology to form the WPTECT probe. The WPT circuit topology acts as a signal-conditioning circuit to the probe excitation and response to enhance detection accuracy at efficient energy transfer and multiple resonance capability.

In the circuit diagrams of WPTECT, the PS-PS topology is utilised as shown in Figure 1. This involves the connection of Ca and Cb capacitors in series and parallel, respectively, to the Tx and Rx coils (L1 and L2) to control the resonance point. The values of Ca and Cb in the primary circuit are the same as those in the secondary circuit. These values are found appropriately from Equations (3.1) and (3.2) to achieve a resonance frequency of 1 MHz, taking into account the natural resonance of the Tx/Rx, the nature of the surface defect, and the limitations of the experimental measuring instrument (a network analyser). Table 2 provides the parameters for the Tx and Rx coils, including the values for the compensating reactance capacitors, Ca and Cb of the probe.

To find the compensating reactance, Xa and Xb, for maximum power transfer, we use the input (rs) and output (RL) characteristic impedances of the VNA, as well as the Tx – Rx DC resistances (R1 and R2). The source, rs, and load, RL, and resistances are constant and equal in our measuring instrument, VNA E5071B. The VNA's characteristic impedance, the real part (Rc) is 50Ω and the imaginary part (Xc) is 0Ω at port1 and port2. The two compensating reactances, jXa and jXb, (see Figure 1) at the resonance frequency, determine the values of the two capacitors, Ca and Cb, respectively. We use expressions (3.1) and (3.2) and the principles of the L-matching network to calculate Xa and Xb reactance values for the PS-PS topology [30]. The PS-PS WPTECT topology probe provides a unique attribute when jXb < jXa; more current passes through the Tx coil for optimal flux linkage, leading to a higher voltage induced in the Rx coil.

$$X_a = -\frac{{R_C}^2 + {X_c}^2}{X_c + QR_c} \tag{3.1}$$

$$X_b = Qr_1 - X_1 \tag{3.2}$$

Table 2. Tx-rx probe configured parameters and experimental variables.

Item	Description	Value
Tx & Rx coils	Inductance, L1 = L2	12.90μH
(Manufacturer Part No.: IWAS3010AZEB130KF1)	Equivalent resistance, R1 = R2	0.70Ω
PS-PS topology	Ca	26.71nf
Matching capacitors	Cb	1.96nf
f0	Design resonance frequency (air)	1.00MHz
Measuring instrument	E5071B, VNA with port1 and port2 having equal characteristics (Xc = 0, Rc = 50 Ω)	
Sweeping frequency	Swept-frequency excitation (1601 frequency points)	1.00MHz –7.00MHz

$$Q = \pm\sqrt{\frac{R_c}{r_1}\left(1 + \left(\frac{X_c}{R_c}\right)^2\right) - 1} \tag{3.3}$$

The probe's ability to identify and measure slots relies on the recorded values of incident and reflected voltages, as well as the frequency characteristics of the scattering transmission (S21) parameters response. This response provides insight into how well the PS-PS WPTECT performs at different experimental frequencies of concern.

3.3. Experimental study

The experimental setup shown in Figure 3(a) consists of WPT-based ECT equipment that uses the VNA (E5071B). It includes an advanced PS-PS topology of the Tx-Rx WPTECT probe, an XYZ scanner and its controller, a fabricated sample for investigation, and a personal computer (PC) for synchronising the XYZ scanner and for data capturing and processing. Meanwhile, Figure 3 (b) and (c) display the photo of the fabricated sample and the Tx-Rx probe arrangement used throughout the study. The Rx coil is placed above the Tx coils coaxially, at a constant axial separation of 0.2 mm, as shown in Figure 3(c). The experimental setup is designed to include connected probes to the VNA, with the Tx unit always being connected to port1 and the Rx unit to port2 for each response measurement in every specific investigation.

This experiment used WPTECT's advanced topology probe to scan two aluminium samples, covering slots S1 to S8. The probe was attached to an XYZ scanner, which moved it axially to scan the four slots in the sample2, with a scan step of 0.2 mm and 1 mm lift-off for each sample. The Tx coil was excited using the Vector Network Analyzer (VNA) E5071B, which provided precise control over the frequency and amplitude of the excitation signal, ensuring accurate and reproducible measurements. After scanning sample2, sample1 was also scanned at the same lift-off distance and scan step for each slot area, starting before the slot edge to a point after the slot. At each scan point, an Agilent RF Network Analyzer was used to measure the S21 response of the PS-PS topology for 1601 frequency points ranging from 1 MHz to 7 MHz. The VNA was set up to provide constant and equal characteristic impedance, allowing only the sample influence to affect the coupling between Tx and Rx coils. The measured S21 responses were collected for further analysis, with the S21 carrying information related to the sample parameters due to the coupling effect between Tx-Rx and the sample. The next section presents an analysis and comparison of feature extraction using resonance points and Machine Learning Gaussian Random Projection (GRP) for mapping to the slot parameters (widths and depths).

4. Results and feature extractions

This section focuses on selecting and extracting features from the results of the WPTECT system response. It uses the Gaussian Random Projection technique to reduce data dimensionally and evaluate and map to surface points for width and depth information. Furthermore, the section analyses and assesses the two highest points from the multiple resonance points characteristics. This includes identifying the lowest point between the

Table 3. Feature comparison information.

	DEPTH FITTINGS, LLSP			WIDTH FITTINGS, LLSW		
Extracted feature source	Feature	R^2-value (%)	RMSE (mm)	Feature	R^2-value (%)	RMSE (mm)
Gaussian Random Projection (GRP)	Ɛ =0.30	99.26	0.27	Ɛ =0.40	99.60	0.10
at three different parameters	Ɛ =0.65	95.89	0.64	Ɛ =0.45	99.86	0.06
	Ɛ =0.99	99.38	0.25	Ɛ =0.95	99.64	0.09
PCA features	PC1	98.65	0.11	PC1	98.91	0.61
Resonance point features	m1	97.27	0.52	m1	95.91	0.32
	f1	97.71	0.48	f1	99.14	0.15
	f0	91.44	0.93	f0	96.10	0.31
				m2	98.29	0.21
	f2	93.73	0.65	f2	99.56	0.10

two peaks of the response signal to map out additional features to crack parameters and comparing their performance to the GRP features. In addition to the feature extraction using the resonance points and the GRP. A PCA feature extraction is also considered for more feature comparison and selection. The procedure for PCA features computation and extraction are discussed in [19]. The computed PCA results in this paper are presented in Table 3, results and discussion section.

4.1. Machine learning–based Gaussian Random Projection (GRP) feature

The GRP is a highly effective method for reducing the dimensions of data by utilising a random matrix to project high-dimensional data into a lower-dimensional space. Compared to other techniques like principal component analysis (PCA) that rely on data-dependent approaches, GRP is both computationally efficient and data-independent, making it an ideal choice for real-time data processing. The foundation of GRP lies in the Johnson-Lindenstrauss Lemma [31], according to this keeping the Euclidean distance preserved between two data points within an arbitrarily small factor eps (ε), it is possible to project n points with samples $X = [x_1, x_2, \ldots, x_n]$ from $R^o \rightarrow R^d$, where o is original dimensionality of datasets and d is the reduced dimension of datasets.

$$(1-\varepsilon)x_i - x_j^2 \leq f(x_i) - f\left(x_j\right)^2 \leq (1+\varepsilon)x_i - x_j^2 \tag{4.1}$$

where x_i and x_j are original features of datasets and $f(x_i)$ and $f\left(x_j\right)$ are from transformed feature space. The reduced dimensionality space should satisfy $d \geq \frac{ln(n)}{\varepsilon^2}$. The GRP reduce the R^odataset dimension to matrix $R^d = {}^1R^T(X)$. Where R^T is the Gaussian random matrix produced by GRP employed in the presented work.

GRP has been utilised in this paper to select features and reduce dimensionality in the experimental data acquired from scanning sample1 and sample2. It is vital to note that GRP has been widely utilised in published works for feature reduction in various applications. An effective approach involves using an ensemble of GRP and fuzzy-c-means [32] for the outlier detection in the data. In [33], an ensemble model is introduced which combines the use of GRP and nearest neighbours classifier to analyse high-dimensional feature space. In a ref [34], a method for gearbox fault diagnosis using

a hyperdisk classifier and GRP is presented. According to [35], a biometric template protection technique using GRP has been proposed for user authentication, which boasts high accuracy and requires less training time. Although GRP is a computationally efficient and data-independent unsupervised learning technique, it is known to be highly unstable due to the potential for vastly different clustering results from varied Gaussian Random Projection technique results. The Eps parameter controls the quality of the embedding according to the Equations (4.1). In this paper, we did an extensive evaluation of hyperparameters (eps) for slot parameter characterisation.

The GRP algorithm is tested with various values of hypermeter (eps) to identify the three most stable reduced data for maximum R-square value and minimum RMSE. The linear fitting curves of the eps parameter extracted features are given in Figures 5(c) and 7(c) for the depth and width reconstruction and discussed in detail in section 4.2. The top three results, with the best R-square values, for depth and width characterisation are also discussed and presented in Table 3.

4.2. Resonance point features

The magnitudes and frequencies of the resonance points and minima points are extracted in this section and presented based on the slot's depth and width parameters characterisation.

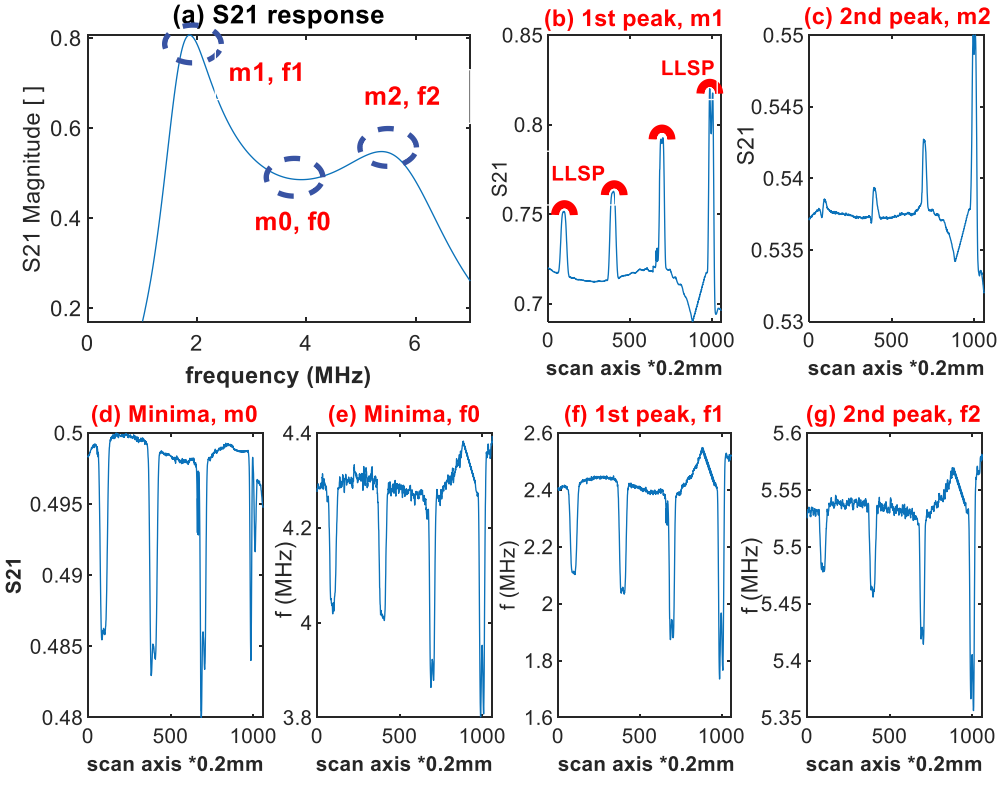

Figure 4. WPTECT System response and extracted features for depth information.

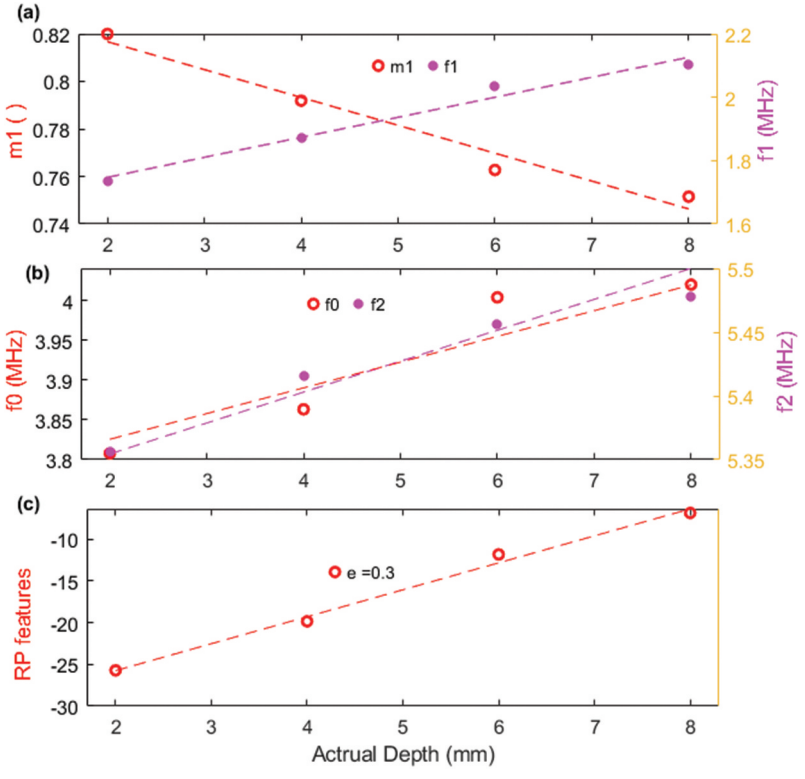

Figure 5. Extracted features versus actual depths (a) first peak magnitude and frequency, m1 and f1 (b) minima and second peak frequencies, f0 and f2 features, and (c) GRP features for control parameters (eps, $\varepsilon = 0.3$).

4.2.1. Slot depth information

In this section, we first extracted resonance point features and then GRP to gather the slot depth information. Six sets of features (m1, f1, m0, f0, m2, and f2) were extracted from the response of scanning sample2, each of which had a peak value at the crack centre, as shown in Figure 4(b-g). The background noise on the extracted features is within the threshold level and does not affect the depth reconstruction because the depth of the crack depends on the peak amplitude of each extracted feature, which is a standard method in ECT quantification [11,19,36,37]. The peak magnitude of each extracted feature along the scan axis is evaluated and defined as the length of the line scan peak (LLSP). The LLSP is a point where the eddy current density has the highest deviation, which is a point at slot position with the highest eddy current density deviation and depends on the magnitude of crack depth and orientation/inclination parameters.

While LLSP has shown potential as a feature parameter for depth evaluation, we observed inconsistencies in the baseline values and instability in the absence of defects. These issues may be attributed to a combination of factors, including defect depth, instrument non-uniformity, and slight uncontrolled movement or shaking of the XYZ scanner. To mitigate these effects and improve accuracy, we

propose enhanced calibration procedures, a multi-parameter approach, and the application of advanced filtering techniques, in future work. These improvements aim to stabilise the measurements and enhance the reliability of LLSP for depth evaluation.

The LLSPs of the four extracted features, m1, f1, f0 and f2 (Figure 4(b,e,f,g)) were used for the evaluation of the depth because they are monotonically related to the increasing depths and were evaluated to quantify the cracks' depths. The depth of the slots decreases from 8 to 2 mm for S5 to S8 slots, respectively, as indicated in Figure 3(b). The LLSPs of the m1, f1, f0 and f2 formed a linear relationship with the actual depths of the slots. Therefore, we created a linear regression model to predict feature depth and determine how well each feature reconstructs the actual slot depth. MATLAB® software was used to compute the model's fitting parameters, R^2-value, and RMSE for the S5 to S8 slots reconstruction.

Figure 5 depicts the linear regression model fitting curves of the m1, f1, f0, and f2 features, including three selected GRP features. The fitting values (R^2-value and RMSE) of the LLSP of the extracted features versus actual depths analysis differentiate the extracted feature capability for slot characterisation compared to the other features. The computed R^2-value and RMSE for the features are presented in Table 3. The LLSP from the GRP feature has the highest goodness of fitting, R^2-value = 99.38%, and minimum RMSE = 0.25 mm at eps = 0.99. The highest reconstruction fitting parameter from the features by the GRP technique is due to its data independence and does not require initial covariance matrix calculation and similarity among data points. Moreover, among the resonance points features, m1 and f1, has a better-predicted depth as indicated by the R^2-value and RMSE because it is more sensitive to sample parameter variation as depicted by Figure 2(a-c), simulated results.

4.2.2. Slot width information

The slot's width depends on the extracted width spatial features along the scan-axis while its angle orientation depends on the spatial feature skewness [36]. In this paper, the slot width parameter quantification is achieved by extracting features along the scan axis from the resonance points of the dual peak response shape of scanning four surface slots (S1 to S4) on sample1, individually at an interval of 0.2 mm scan step and 1 mm lift-off distance. Therefore, the extracted features from scanning four slots were normalised using min-max normalisation, [0 1] scale for same scale comparison and to remove the influence of the maximum (or minimum) amplitude variation which contains slot depth information. Figure 6 shows the normalised first peak features of the four slots (a) m1 (magnitude) features with a maximum value at the centre of the slot, and (b) f1 (frequency) features of the four slots' response with a minimum value at the centre of the slot. The second response peak extracted features, including GRP, are either ascend or descend to the centre of the slot similar to the first peak features in Figure 6. For optimal width parameter extraction, 70% of its maximum/minimum value along the spatial (scan) axis is considered, as presented in ref [17]. The 70% position of the normalised m1 and f1 width features are indicated in Figure. 6(a,b), respectively which is described as LLSW (Length of Line Scan Width) as the length between the two spatial (scan axis) points.

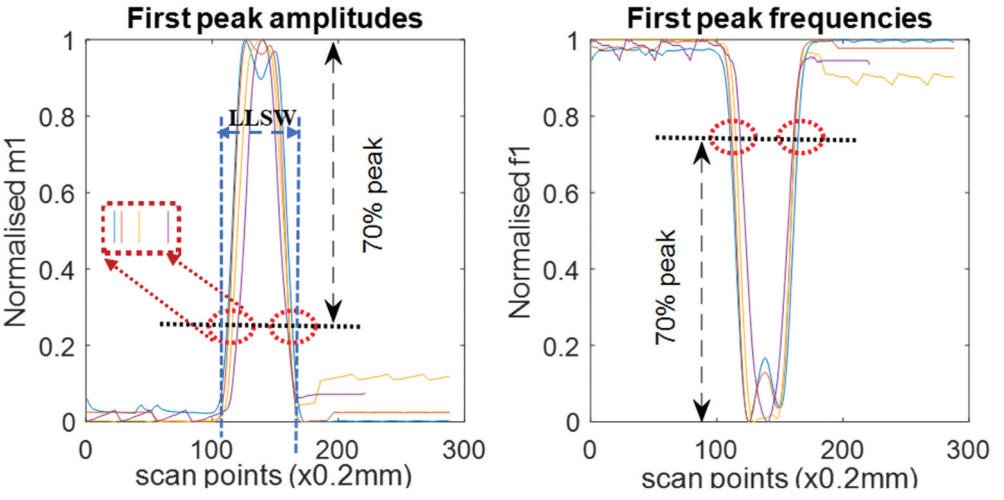

Figure 6. Normalised width first peak features showing the position of LLSW features.

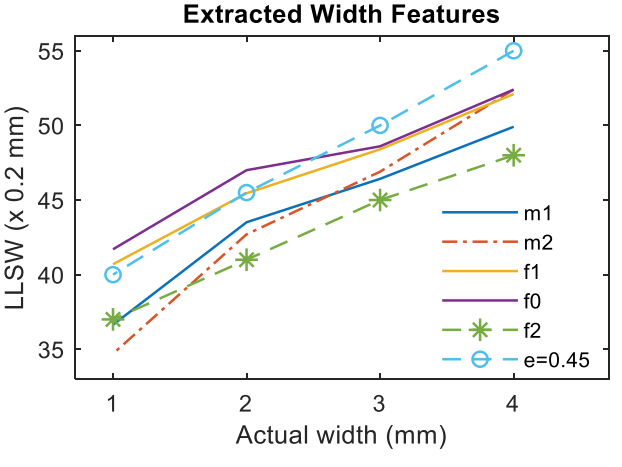

Figure 7. Extracted LLSW features (m1, m2, f1, f0, f2 and eps = 0.45) versus widths.

Figure 7 shows the six extracted LLSW features against the actual slot widths. The LLSW are obtained from both the resonance point features (m1, m2, f1, f0 and f2) with a monotonic relationship with the width parameter and the GRP features for width quantification at eps = 0.45. The combined plot of the six sets of features in Figure 7 allows for a direct comparison of the impact of resonance points and GRP extracted LLSW features on the slot width.

The LLSW characteristics increase with the widening of the slot because it represents the intervals between points where the eddy current density has the highest deviation. Therefore, the width of the slot depends on the length between two points where eddy current density is highest, while the depth of the slot impacts the amplitude of the resonance point features and that of some GRP extracted features. The two points with

the highest eddy current density depend on the crack opening inclination/orientation [36,38].

To determine the width of the slot, a linear regression model is utilised to calculate the regression model parameters, R^2-value, and RMSE for correlating LLSW to the actual slot width parameter. The results of the R^2-values and RMSE are provided and discussed in the next section.

5. Results and discussion

In this section, we present and discuss the results obtained from the experimental study. Also, the section compares the extracted resonance point features from the response of scanning the two aluminium samples for performance analysis of the methods on slot characterisation, including GRP extracted features. Additionally, the proposed method is compared with the state-of-the-art literature on slot/crack quantitative evaluation.

5.1. GRP features comparison with other features

A dimensionality reduction method called the Gaussian Random Projection (GRP) algorithm works by randomly projecting high-dimensional data onto a lower-dimensional environment using a random matrix considered for feature projection to the spatial domain. The eps parameter ($0 < \varepsilon < 1$) controls the distortion in the pairwise distances between the original and projected data points. The GRP focuses on maintaining pairwise distances between data points in the reduced space. In contrast, techniques like PCA or autoencoders directly strive at data reconstruction. Although not specifically aimed at reconstruction fitting, GRP's capacity to preserve structural information by preserving point-to-point distances can help improve reconstruction quality indirectly by lowering noise or superfluous features, possibly boosting the performance of succeeding models. However, depending on variables like data dimensionality, noise levels, and particular problem situations, its effect on reconstruction fitting differs. As a result, its usefulness needs to be evaluated in the context of the overall data analysis.

However, the use of lesser ε values could result in higher processing demands and the conservative preservation of superfluous information, which could lead to inefficiency or overfitting. It is important to strike a balance between minimising distortion and computational feasibility; the choice of ε depends on the particular application and the intended trade-off between computational efficiency and accuracy. To find the ideal ε for reaching the necessary balance in the setting, experimentation and validation are still essential. A lower ε means less distortion and more accuracy, but also more computational cost. The three best different values (lower, middle, and upper) of ε are chosen with the best R^2-value for presentation.

Table 3 shows the comparison of the slots' width and depth fitting results of the extracted features. The GRP at three selected different eps (ε) parameters are compared with the extracted resonance point features. The resonance point features, which extract features based on the resonance frequency and amplitude of the response signal are extracted. The features are m1, f1, m0, f0, m2 and f2, as shown in Figure 4 where m stands for amplitude and f stands for frequency. The subscript shows the order of the resonance peak, with 0 being the fundamental frequency and 1 and 2 being the first and second

harmonics. Additionally, principal component analysis (PCA) features from the response shape are considered in this comparison. The application of PCA for feature reduction to the spatial domain was demonstrated in our previous paper [17], including its computation algorithm flow chart [19]. The computed PCA feature relies on the response shape, and it is included in Table 3 for more feature comparison. In this comparison, the first principal component (PC1) is selected because it has the highest percentage deviation around the slot area compared to other PCs.

The table also shows the R^2-value and RMSE for each feature, which are measures of how well the feature predicts the shape of the fittings. The R^2-value is the coefficient of determination, which ranges from 0 to 100% and indicates how much of the variation in the shape is explained by the feature. The RMSE is the root mean squared error, which measures the average difference between the predicted and actual shape. A higher R^2 value and a lower RMSE mean better performance.

The slot characterisation using GRP feature reduction provides the best reconstruction fitting compared to PCA and resonance point features with an R^2-value of 99.38% for the depth and 99.86% for the width at 0.25 mm and 0.06 mm, respectively. The Resonance point feature performance for the depth characterisation is less than that of the PCA feature. However, the first frequency feature from the Resonance point features is far better than the PCA feature for width characterisation.

5.2. Comparison with state-of-the-art defect characterisation

The proposed WPT-based ECT method is further compared with the current state-of-the-art defect characterisation in terms of R^2-value and RMSE for slot/crack parameter reconstruction. The proposed technique is applied to the evaluation of slot parameters on aluminium material. The performance comparison of this technique with other techniques for different materials with slot/crack defects is summarised in Table 4.

As presented in Table 4, most of the published NDT&E for crack quantification articles varied the crack parameter to be quantified, while other parameters were

Table 4. Comparison for crack parameters reconstruction.

Year, Sample	Reference	Note	Maximum R^2 (min RMSE)	Methods	Quantified parameter
2019 Aluminium block	N. Faris [36]	Quantified depths at constant width (0.3mm) and angles. Quantified angle at constant width (0.3mm) and depths. Features: skewness, length of line scan (LLS), and the maximum length of line scan (LSmax).	Depth, Angle: **99.20%, 99.70%** (0.20mm, 2.9°) respectively.	Pulse ECT	Depth and Angle
2021 Aluminium cladding	A Sophian [39]	Thickness evaluation due to corrosion. Features: Response decay coefficient & Machine Learning based Gaussian process regression (GPR) algorithm	**94.20%** (0.27mm)	Pulsed-ECT	Thickness (Corrosion)
2023 Aluminium	Our proposed probe	Quantified depths, and widths parameters. Features: GRP	Depth & width: **99.38**% (0.25mm) & **99.86**% (0.06mm)	WPT-based ECT	Depth and width

considered as constant as described in [36,40–42]. In real applications, the peak value of the system response is affected by the crack parameters. The obtained R^2-values in our manuscript are comparable to other NDT&E studies, as shown in Table 4. The improved performance of quantitative results from refs [40,42] may be attributed to the high spatial resolution of modern thermographic cameras, which allows for the detection of micro-surface temperature variation. Additionally, the samples used in these references might have had cracks with a single variable parameter.

However, their R^2 values are as good as those obtained in this proposed work. Similarly, the better performance results from the Pulsed- -ECT in ref [36] were due to the broad frequency potential of the pulse excitation, which covers from the zero frequency to above the fundamental frequency of the harmonics. However, the Pulsed ECT suffer sensitivity to lift-off distance and reduced resolution, which necessitates the requirement for optimising the gap between Tx and Rx and inspection lift-off [43].

Our proposed advanced PS-PS topology of WPTECT quantified the width and depth parameters from the extracted resonance point features and feature extraction using Gaussian Random Projection (GRP). The peak of the extracted features around the crack and the width of the feature taken from the 70% peak point defined the depth and width of the crack, respectively. The proposed PS-PS topology of WPTECT shows exclusively good application attributes to quantitative NDT&E of depth parameter with R2-value of 99.38% at 0.25 mm RMSE and width with 99.86% and 0.06 mm. Furthermore, it can operate in scanning and non-scanning mode due to its simplicity in structure and sweeping excitation signal and it has the availability of a cheap WPT IC chip for signal processing to replace VNA in real-life applications with its inexpensive probe.

The proposed topology of WPTECT provides various features for multiple slot parameters. The extracted features' shape along the scan axis indicates the LLSW, which only contains data about the width parameter. Conversely, the peak position of the feature determines the actual location of the slot, while the magnitude of the feature at the peak position indicates the depth of the slot. The peak of the extracted feature occurs due to a decrease in sample conductivity around the slot, which results in higher eddy current density. The shape of the feature depends on the gap between the two points where the eddy current density concentration is higher.

The current results for slot depth and width detection show promise, but further improvements are needed to reach the precision of commercial instruments. The proposed advanced circuit topology of the WPTECT system is limited to metallic materials and their defect detection and characterisation. Future research will focus on miniaturising the system into a portable form and integrating it into an IoT platform for real-time structural integrity monitoring. Additionally, we plan to optimise sensor design and incorporate advanced machine-learning techniques for better signal processing. The proposed system offers unique advantages, such as efficient power transfer and flexibility in real-time applications, making it a promising technology for various industrial NDT&E applications.

6. Conclusion

The paper proposes a method for multiple feature extraction at efficient energy transfer response from the splitting resonance response of the WPT-based ECT including

features from the GRP of the system response. The WPT provides multiple feature points at maximum energy transfer, leading to better evaluation performance of the slot parameters.

In comparison with other ECT techniques, there are more diverse Integrated Circuit chips for WPT signal processing, making it a better choice for real-life applications. The depth and width of the slot on aluminium material have been characterised from the experimental study, achieving higher R^2-value and lower RMSE using the GRP features from the response of the proposed inexpensive Tx-Rx WPTECT probe. This has been compared to other ECT of NDT&E techniques.

The proposed WPT-based ECT overcome the challenges of the ECT probe in achieving maximum energy transfer response with multiple parameter information due to splitting resonance frequency behaviour and swept frequency excitation. Additionally, the novel GRP feature extraction techniques employed in WPTECT have achieved higher R^2-values for the slot parameters.

In future work, the proposed system will be applied for a higher spacing (lift-off) inspection [44] with a time series and other signal compression analysis for higher SNR values [45], including lift-off compensation for real-time inspection.

Disclosure statement

No potential conflict of interest was reported by the author(s).

Funding

Federal Ministry of Petroleum Resources >Petroleum Technology Development Fund [PTDF/ED/PHD/DLU/1276/17].

ORCID

Lawal Umar Daura http://orcid.org/0000-0002-2468-4369
Gui Yun Tian http://orcid.org/0000-0002-7563-1523

References

[1] Lu K. The future of metals. Science. 2010;328(5976):319–320. doi: 10.1126/science.1185866
[2] Findlay SJ, Harrison ND. Why aircraft fail. Mater Today. 2002;5(11):18–25. doi: 10.1016/S1369-7021(02)01138-0
[3] Sophian A, Tian GY, Taylor D, et al. Electromagnetic and eddy current NDT: a review. Insight Non Destr Test Cond Monit. 2001;43(5):302–306.
[4] Liao Z, Sun Y, Ye Z, et al. Resonant analysis of magnetic coupling wireless power transfer systems. IEEE Trans Power Electron. 2019;34(6):5513–5523. doi: 10.1109/TPEL.2018.2868727
[5] Wu C, Zhang Z, Cheng X, et al. An integrated multimode battery charger in a qi compliant wireless power receiver. Analog Integr Circ Sig Process. 2020;103(3):425–434. doi: 10.1007/s10470-019-01582-z
[6] Kurs A, Karalis A, Moffatt R, et al. Wireless power transfer via strongly coupled magnetic resonances. Science. 2007;317(5834):83. doi: 10.1126/science.1143254

[7] Daura LU. Investigation of wireless power transfer-based eddy current non-destructive testing and evaluation [PhD thesis]. School of Engineering, Newcastle University; 2022. http://theses.ncl.ac.uk/jspui/handle/10443/5641
[8] Tesfalem H, Fletcher AD, Brown M, et al. Study of asymmetric gradiometer sensor configurations for eddy current based non-destructive testing in an industrial environment. NDT E Int. 2018;100:1–10. doi: 10.1016/j.ndteint.2018.07.007
[9] Morozov M, Tian GY, Edgar D. Comparison of pec and sfec nde techniques. Nondestr Test Evaluation. 2009;24(1–2):153–164. doi: 10.1080/10589750802195543
[10] Sophian A, Tian GY, Fan M. Pulsed Eddy current non-destructive testing and evaluation: a review. Chin J Mech Eng. 2017;30(3):500–514. doi: 10.1007/s10033-017-0122-4
[11] Janousek L, Stubendekova A, Smetana M. Novel insight into swept frequency eddy-current non-destructive evaluation of material defects. Measurement. 2018;116:246–250. doi: 10.1016/j.measurement.2017.11.039
[12] Stubendekova A, Janousek L. Influence of selected defect parameter on response signals in swept frequency electromagnetic nondestructive testing. In: 2016 ELEKTRO; 2016. p. 593–596. [2016 May 16–18]. doi: 10.1109/ELEKTRO.2016.7512146
[13] Mao X, Lei Y. Thickness measurement of metal pipe using swept-frequency eddy current testing. NDT E Int. 2016;78:10–19. doi: 10.1016/j.ndteint.2015.11.001
[14] Tai C-C. Characterization of coatings on magnetic metal using the swept-frequency eddy current method. Rev Sci Instruments. 2000;71(8):3161–3167. doi: 10.1063/1.1304862
[15] Svatos J, Vedral J. The usage of frequency swept signals for metal detection. IEEE Trans Magn. 2012;48(4):1501–1504. doi: 10.1109/TMAG.2011.2173174
[16] Hughes RR, Dixon S. Performance analysis of single-frequency near electrical resonance signal enhancement (SF-NERSE) defect detection. NDT E Int. 2019;102:96–103. doi: 10.1016/j.ndteint.2018.11.008
[17] Daura LU, Tian GY. Characterization of angular RCF cracks in a railway using modified topology of WPT-Based eddy current testing. IEEE Trans Ind Inf. 2023;19(4):5612–5622. doi: 10.1109/TII.2022.3201587
[18] Daura LU, Tian GY, Yi Q, et al. Wireless power transfer-based eddy current non-destructive testing using a flexible printed coil array. Phil Trans R Soc A. 2020;378(2182):20190579. doi: 10.1098/rsta.2019.0579
[19] Daura LU, Tian GY. Wireless power transfer based non-destructive evaluation of cracks in aluminum material. IEEE Sensors J. 2019;19(22):10529–10536. doi: 10.1109/JSEN.2019.2930738
[20] Machura P, Li Q. A critical review on wireless charging for electric vehicles. Renewable Sustain Energy Rev. 2019;104:209–234. doi: 10.1016/j.rser.2019.01.027
[21] Zhang Z, Pang H, Georgiadis A, et al. Wireless power transfer—an overview. IEEE Trans Ind Electron. 2019;66(2):1044–1058. doi: 10.1109/TIE.2018.2835378
[22] Shevchenko V, Husev O, Strzelecki R, et al. Compensation topologies in IPT systems: standards, requirements, classification, analysis, comparison and application. IEEE Access. 2019;7:120559–120580. doi: 10.1109/ACCESS.2019.2937891
[23] Chwei-Sen W, Stielau OH, Covic GA. Design considerations for a contactless electric vehicle battery charger. IEEE Trans Ind Electron. 2005;52(5):1308–1314. doi: 10.1109/TIE.2005.855672
[24] Chwei-Sen W, Covic GA, Stielau OH. Power transfer capability and bifurcation phenomena of loosely coupled inductive power transfer systems. IEEE Trans Ind Electron. 2004;51(1):148–157. doi: 10.1109/TIE.2003.822038
[25] Zhang Y, Yan Z, Zhu J, et al. A review of foreign object detection (FOD) for inductive power transfer systems. eTransportation. 2019;1:100002. doi: 10.1016/j.etran.2019.04.002
[26] Samanta S, Rathore AK. A comparison and performance evaluation of L-C and C-C-L compensation schemes on CSI based inductive WPT application. In: 2016 IEEE 25th International Symposium on Industrial Electronics (ISIE); 2016. p. 817–822. [2016 Jun 8–10]. doi: 10.1109/ISIE.2016.7744995

[27] Zhuang Y, Chen A, Xu C, et al. Range-adaptive wireless power transfer based on differential coupling using multiple Bi-directional coils. In: IEEE Transactions on Industrial Electronics; 2019. p. 7519–7528. doi: 10.1109/TIE.2019.2945304
[28] Zhang Y, Zhao Z. Frequency splitting analysis of two-coil resonant wireless power transfer. Antennas Wirel Propag Lett. 2014;13:400–402. doi: 10.1109/LAWP.2014.2307924
[29] Liao ZJ, Ma S, Feng QK, et al. Frequency splitting elimination and utilization in magnetic coupling wireless power transfer systems. In: IEEE Transactions on Circuits and Systems I: Regular Papers; 2020. p. 1–11. doi: 10.1109/TCSI.2020.3040750
[30] Shi W, Chen W, Lu C, et al. Optimal design of spiral coil EMATs for improving their pulse compression effect. J Nondestruct Eval. 2021;40(2):38. doi: 10.1007/s10921-021-00771-z
[31] Larsen KG, Nelson J. Optimality of the Johnson-Lindenstrauss Lemma. In: 2017 IEEE 58th Annual Symposium on Foundations of Computer Science (FOCS); 2017. p. 633–638. [2017 Oct 15–17]. doi: 10.1109/FOCS.2017.64
[32] Shi Z, Chen L, Duan J, et al. Robust and fuzzy ensemble framework via spectral learning for random projection-based fuzzy-c-means clustering. Eng Appl Artif Intel. 2023;117:105541. doi: 10.1016/j.engappai.2022.105541
[33] Deegalla S, Walgama K, Papapetrou P, et al. Random subspace and random projection nearest neighbor ensembles for high dimensional data. Expert Syst Appl. 2022;191:116078. doi: 10.1016/j.eswa.2021.116078
[34] Zhu Z, Yang Y, Hu N, et al. Sparse random projection-based hyperdisk classifier for bevel gearbox fault diagnosis. Adv Eng Inf. 2022;53:101713. doi: 10.1016/j.aei.2022.101713
[35] Yang W, Wang S, Shahzad M, et al. A cancelable biometric authentication system based on feature-adaptive random projection. J Inf Secur Appl. 2021;58:102704. doi: 10.1016/j.jisa.2020.102704
[36] Nafiah F, Sophian A, Khan MR, et al. Quantitative evaluation of crack depths and angles for pulsed eddy current non-destructive testing. NDT E Int. 2019;102:180–188. doi: 10.1016/j.ndteint.2018.11.019
[37] Nafiah F, Sophian A, Khan MR, et al. Image-based feature extraction technique for inclined crack quantification using pulsed eddy current. Chin J Mech Eng. 2019;32(1):1–9. doi: 10.1186/s10033-019-0341-y
[38] Zhang W, Chen G, Pang W. Shannon information entropy of eddy current density distribution. Nondestr Test Evaluation. 2017;32(2):152–165. doi: 10.1080/10589759.2016.1184266
[39] Sophian A, Nafiah F, Gunawan TS, et al. Machine-learning-based evaluation of corrosion under insulation in ferromagnetic structures. IIUM Eng J. 2021;22(2):226–233, 07/04. doi: 10.31436/iiumej.v22i2.1692
[40] Zhu J, Tian GY, Min Q, et al. Comparison study of different features for pocket length quantification of angular defects using eddy current pulsed thermography. IEEE Trans Instrum Meas. 2019;68(5):1373–1381. doi: 10.1109/TIM.2018.2890053
[41] Zhu J, Min Q, Wu J, et al. Probability of detection for eddy current pulsed thermography of angular defect quantification. IEEE Trans Ind Inf. 2018;14(12):5658–5666. doi: 10.1109/TII.2018.2866443
[42] Xia H, Wu J, Xu Z, et al. Defect visualization and depth quantification in scanning induction thermography. IEEE Sensors J. 2021;21(9):10437–10444. doi: 10.1109/JSEN.2021.3060916
[43] Ona DI, Tian GY, Sutthaweekul R, et al. Design and optimisation of mutual inductance based pulsed eddy current probe. Measurement. 2019;144:402–409. doi: 10.1016/j.measurement.2019.04.091
[44] Zhang X, Meng H, Wei B, et al. An improved three-coil wireless power link to increase spacing distance and power for magnetic resonant coupling system. EURASIP J Wireless Commun Netw. 2018;2018(1):131. doi: 10.1186/s13638-018-1148-8
[45] Ye C, Laureti S, Malekmohammadi H, et al. Swept-frequency eddy current excitation for TMR array sensor and pulse-compression: feasibility study and quantitative comparison of time and frequency domains processing. Measurement. 2022;187:110249. doi: 10.1016/j.measurement.2021.110249